

Two-Dimensional Autonomous Micro-Particle Manipulation Strategies for Magnetic Micro-Robots in Fluidic Environments

Chytra Pawashe, Steven Floyd, *Member, IEEE*, Eric Diller, *Student Member, IEEE*, and Metin Sitti, *Senior Member, IEEE*

Abstract—This work develops autonomous manipulation strategies for a mobile untethered micro-robot that operates on a 2-D surface in a fluidic environment. The micro-robot, which is a permanent magnet, is under 500 μm in all dimensions and is actuated by oscillating external magnetic fields. Two types of manipulations are considered: (1) front-pushing, where the micro-robot pushes a micro-object by direct contact, and (2) side-pushing, which can result in non-contact pushing where the fluid flow fields generated by a translating micro-robot are used to displace a micro-object. Physical models are provided to estimate the displacement of the micro-object due to the fluid motion. Model-based controllers to perform contact and non-contact manipulation are proposed, which iteratively correct emerging manipulation behaviors to improve performance. It is found that using a model-based solution as a feed-forward input, combined with a learning controller, can significantly improve micro-object pushing performance. Finally, we begin to address the problem of assembling two micro-objects together using the micro-robot, which is only successful by using a side-pushing method.

Index terms - Micro/nano-robots, micro/nano-manipulation, autonomous control

I. INTRODUCTION

Sub-millimeter sized robots, or micro-robots, have potential future applications in areas such as biomedicine [1], [2]. These micro-robots have necessitated new approaches to power delivery and control at the micro-scale. The current designs in literature, including electrostatic [3], [4], electromagnetic [5]–[9], optical [10], laser driven thermal impact [11], chemical [12], and bacteria-propelled systems [13]–[15], have resulted in successful wireless control of individual mobile micro-robots. Due to requirements for an external powering and control system, these micro-robots are in fact the *untethered micro-scale end-effector* of a robotic system.

Many of these micro-robotic systems can be used to manipulate micro-objects in their environments, and are usually operated in fluidic environments, often due to environmental requirements of the micro-robots themselves [5], [6], [10], [13]. Operating in a fluid provides the advantage of reduced adhesion and friction between surfaces, both of which can

make manipulation tasks difficult. Because fluid flows can be generated in fluidic environments, micro-object manipulations can occur without end-effector contact [16], which can be useful for the manipulation of fragile objects, and for precise positioning.

Compared to traditional micro-manipulation tools such as micro-grippers, untethered micro-robots have the advantage of being able to operate in enclosed environments, while maintaining physical presence. Micro-robotic systems such as [3], [5], [6], [17], [18] can also support multiple untethered end-effectors. These features can lead to potential applications in micro-fluidic, bio-manipulation, and micro-assembly systems.

In our previous work [8] we developed a micro-robot platform that allows a sub-millimeter magnetic micro-robot to be wirelessly controlled on a 2-D surface by using oscillating electromagnetic fields applied externally. In [19], we investigated using the micro-robot to manipulate micro-objects in a fluid, and analyzed the effects on the micro-objects from the fluid flow caused by a translating micro-robot. In this work, we apply the physical manipulation models from [19] towards the development of efficient autonomous micro-object manipulation controllers, and focus primarily on contact and non-contact-based pushing by a micro-robot under fluid. Additionally, a method to push together two micro-objects together under a fluid using a micro-robot is demonstrated, which supports the feasibility of this method for future complex assembly tasks.

This paper is divided as follows: Section II discusses the magnetic micro-robot system, with a description of the manipulation problem in Section III. An overview of the relevant physics of micro-object manipulation is discussed in Section IV, and manipulation strategies are proposed in Section V. Experiments and discussion of the manipulation strategies are provided in Section VI, with conclusions and future work discussed in Section VII.

II. MAGNETIC MICRO-ROBOT SYSTEM

The magnetic micro-robot (Mag- μ Bot) is actuated by six independent electromagnetic coils by utilizing oscillating applied magnetic fields, resulting in stick-slip motion on a 2-D surface; this system is described in our prior works [8], [17]–[19]. The Mag- μ Bot is capable of operating on arbitrary nonmagnetic, low adhesion surfaces. Additionally, Mag- μ Bots can operate in gases and liquids of up to about 50 cSt.

C. Pawashe was with the Department of Mechanical Engineering, Carnegie Mellon University. He is now at Intel Corporation, Hillsboro, OR, USA.

S. Floyd was with the Department of Mechanical Engineering, Carnegie Mellon University. He is now a staff engineer with Areté Associates, Arlington, VA 22202, USA.

E. Diller and M. Sitti are with the Department of Mechanical Engineering, Carnegie Mellon University, Pittsburgh, PA 15213, USA sitti@cmu.edu

Mag- μ Bots are fabricated in a batch process using a molding technique presented in [20]. They are composed of neodymium-iron-boron (NdFeB) particles (Magnequench MQP-15-7) suspended in a polyurethane matrix (TC-892, BJB enterprises), and can be fabricated to arbitrary planar geometries. In this work, a star-shaped Mag- μ Bot is used with characteristic dimensions $310 \times 480 \times 130 \mu\text{m}^3$, shown in Fig. 1; this geometry is useful for object manipulation tasks due to the concave forward face, which can capture objects. Polystyrene micro-spheres with diameter $210 \mu\text{m}$ (PS-DVB, Duke Scientific Inc.) are used in this study as the objects for the Mag- μ Bot to manipulate. Experiments are performed on a glass surface in a silicone oil environment (Dow Corning 200 fluid, 20 cSt).

For autonomous control of Mag- μ Bots, a particle filter algorithm [21] is implemented to track the positions of objects using the visual feedback information from the camera. This algorithm primarily operates on the gradient of the image, and is capable of reliably tracking Mag- μ Bots and manipulatable objects at 30 frames/sec. Visual servoing of the Mag- μ Bot is achieved by a basic proportional-integrating controller, which aims to reduce the error between the micro-robot and its target position by varying its velocity and heading. Path planning is performed by a Wavefront algorithm [22], which allows the micro-robot to avoid relevant obstacles appropriately.

III. MICRO-OBJECT MANIPULATION AND ASSEMBLY

Within a fluid, a translating Mag- μ Bot generates flow fields, which interact with other objects in the fluid, and can be used to manipulate them. Because of the low Reynold's number (below 0.01), the flow effects act at relatively large distances, and inertial effects are negligible. Therefore, the velocity of the micro-robot is unimportant; rather, the position of the micro-robot dictates the fluid interaction with a micro-object. Two modes of manipulation are considered: contact manipulation, and non-contact manipulation.

Figure 1 shows a Mag- μ Bot pushing a micro-sphere from the front, resulting in contact-manipulation. The flow field generated by the Mag- μ Bot initially displaces the micro-sphere D_p before contact manipulation begins. Once the sphere is pushed to a desired location, the Mag- μ Bot must leave the area. However, due to fluid flow, the micro-robot leaving will displace the micro-sphere a distance $D_{p,r}$. Thus, to enable accurate positioning of a micro-object by contact manipulation, $D_{p,r}$ must be determined and compensated for.

Figure 2 displays a Mag- μ Bot pushing a micro-sphere from the side. D_g is the initial gap distance between the Mag- μ Bot and sphere, and D_s is the displacement of the sphere caused by the induced flow fields as the Mag- μ Bot passes by. If D_g is sufficiently large, the Mag- μ Bot will not contact the sphere yet still displace it due to the fluid effects. To enable the accurate and efficient positioning of a micro-object using this manipulation method, a relation must be determined between D_g and D_s .

To achieve the assembly of multiple micro-objects, a Mag- μ Bot must push one of the objects to the other so that they contact. However, due to fluid effects, this task cannot be

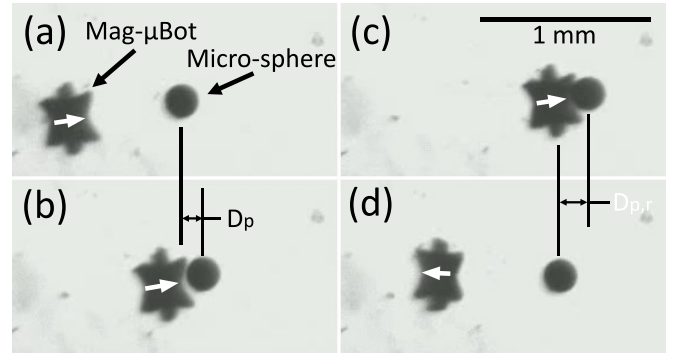


Fig. 1. (a) A teleoperated star-shaped Mag- μ Bot and a $210 \mu\text{m}$ micro-sphere ready for contact manipulation under liquid on a glass surface. (b) The Mag- μ Bot approaches and contacts the micro-sphere, which displaces before contact occurs. (c) The micro-sphere is pushed further by direct contact. (d) The Mag- μ Bot moves away from the micro-sphere, causing micro-sphere displacement due to fluid interactions. Arrow on Mag- μ Bot indicates direction of its motion.

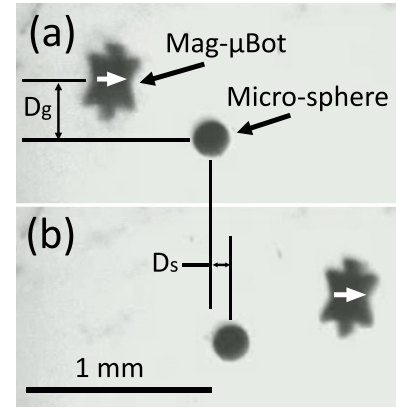


Fig. 2. (a) A teleoperated star-shaped Mag- μ Bot and a $210 \mu\text{m}$ micro-sphere ready for side-pushing under liquid on a glass surface. (b) The Mag- μ Bot moves past the micro-sphere from its side, causing the sphere to displace a small amount, primarily due to the fluid interactions. Arrow on Mag- μ Bot indicates direction of its motion.

achieved by simple contact pushing, as shown in Fig. 3. A pushing method that compensates for this fluid effect is necessary to achieve assembly.

IV. PHYSICAL MODELING

When a Mag- μ Bot manipulates a micro-sphere, the sphere experiences forces from the environment. Figure 4 displays a schematic of these forces, which includes the micro-robot's contact pushing force (F_c), fluid drag forces from the environment ($F(U, u)$), friction forces from the surface (F_f), adhesion forces between the sphere and surface (P), as well as the sphere's own weight (W_b). In this study we primarily focus on manipulations due to fluid interactions, thus ignore F_c in analyses. We develop much of the theoretical background of these interactions in [19], and summarize the formulations in this section.

A. Surface Forces

A micro-sphere on a surface can experience an adhesive force, which primarily is a combination of van der Waals

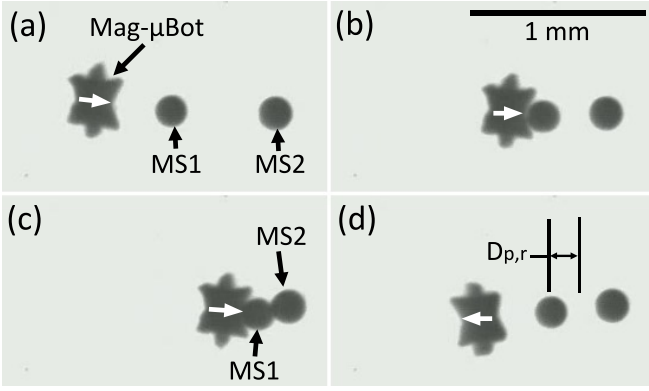


Fig. 3. (a) A teleoperated star-shaped Mag- μ Bot and two micro-spheres, MS1 and MS2, ready for assembly. (b) The Mag- μ Bot moves to the right and front-pushes MS1 towards MS2. (c) MS1 and MS2 are assembled. (d) The Mag- μ Bot retracts from the assembly, and as a result, displaces MS1 by $D_{p,r}$ due to fluid effects. Arrow on Mag- μ Bot indicates direction of its motion.

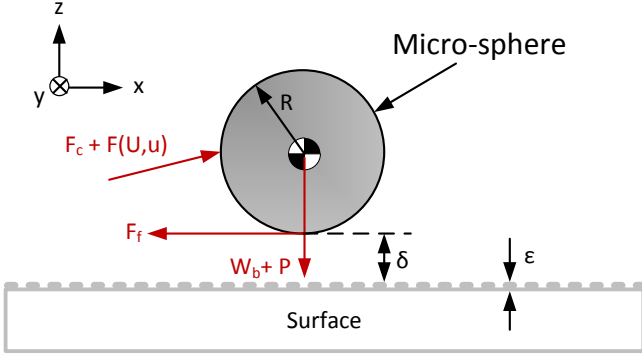


Fig. 4. A free body diagram of a micro-sphere in its environment.

interactions, capillary effects, and electrostatic charging [23]. Capillary forces can be neglected since the entire environment is submerged in fluid, and electrostatic effects are usually small compared to van der Waals [24], [25]. To determine the van der Waals energy density between a micro-object of material 1, a surface of material 2, in a fluid environment 3, the work of adhesion, W_{132} , can be determined using the intrinsic surface energies of the materials, γ_1 , γ_2 , and γ_3 [25], [26]:

$$W_{jk} \approx 2\sqrt{\gamma_j\gamma_k} \quad (1)$$

$$W_{132} = W_{12} + W_{33} - W_{13} - W_{23} \quad (2)$$

where the subscripts j and k correspond to the relevant materials 1, 2, or 3. If W_{132} is positive, materials 1 and 2 will attract, while negative values of W_{132} imply repulsion.

Adhesion modeling for micro- and nano-particle manipulation is discussed in [25], [27], and the adhesive force P of a perfect sphere on a flat surface can be estimated using the Johnson-Kendall-Roberts (JKR) model. P is determined as:

$$P = 1.5\pi RW_{132} \quad (3)$$

where R is the sphere's radius. Values of relevant properties for materials used in this work are given in Table I.

	Surface Energy (γ) [mJ \cdot m $^{-2}$]	Density (ρ) [kg \cdot m $^{-3}$]
Glass	83-280 [28]-[31]	n/a
Polystyrene	33-40 [26], [32]	1060
Silicone Oil	19.8-21 [33], [34]	935

TABLE I
PROPERTIES OF MATERIALS

Due to the wide range of possible surface energies for glass given in Table I, there is a large range of pull-off forces that can potentially exist for a sphere contacting glass under silicone oil. For the $R = 105 \mu\text{m}$ polystyrene micro-spheres used in the experiments, $5.2 \mu\text{N} < P < 23 \mu\text{N}$.

A micro-sphere on a surface in a liquid environment can also experience a friction force (F_f), which can be due to viscous shear in the fluid between the micro-sphere and the surface as it translates. However if the micro-sphere's velocity is very small, *boundary lubrication* can occur. In this case, the friction force can be very high, as fluid layers between the micro-sphere and surface can act more solid-like. Determining the boundary lubrication properties can be highly complicated and is not well understood [35], thus we do not consider it for initial analysis. F_f is implicitly determined in the next section; it is contained in the fluid drag forces exerted on the micro-sphere.

B. Viscous Drag

The displacement of fluid caused by the micro-robot's motion induces drag forces onto micro-objects in the environment. To determine the forces exerted by this flow, the wall-effect due to the surface must be considered, which we analyze in [19]. These forces were first calculated by Goldman et al. [36], [37], and can be used to determine the near-wall fluid forces (F_G) acting on the sphere:

$$\begin{aligned}
 F_G &= 6\pi\mu R \times \\
 &\quad (U_{ip}F_{shear}^* + V_p F_{trans}^* + \Omega R F_{rot}^*) \\
 F_{shear}^* &= 1 + 0.7005 \frac{R}{h} \\
 F_{trans}^* &= \frac{8}{15} \ln \left(\frac{\delta + \epsilon}{R} \right) - 0.9588 \\
 F_{rot}^* &= -\frac{2}{15} \ln \left(\frac{\delta + \epsilon}{R} \right) - 0.2526 \quad (4)
 \end{aligned}$$

where U_{ip} is the in-plane fluid velocity at the sphere's center (relative to the wall), and Ω is the angular velocity of the sphere's rotation, where the axis of rotation is assumed parallel to the plane. Also, $h = R + \delta + \epsilon$ is the distance from the center of the sphere to the no-slip boundary condition, which is dependent upon δ , the distance between the edge of the sphere and the ground, and $\epsilon \approx 25 \text{ nm}$, which is the measured combined characteristic roughness of the two surfaces. Each of the logarithm terms in (4) is appropriately bounded, i.e. $F_{trans}^* < -1$, $F_{rot}^* > 0$. The angular velocity can be related to the translational velocity and the distance from the wall by

fitting a curve to the numerical results of [36] and bounding it to $0 \leq \Omega \leq 0.5676 V_p/R$, which results in:

$$\Omega = (-2.375 \times 10^{-6} e^{12.05R/h} + 1.025 e^{-.1438R/h}) \frac{V_p}{R} \quad (5)$$

To determine the motion of a sphere in a fluid flow, dynamic relations for the sphere are developed, and are used in the simulations:

$$m\ddot{x} = F_G(U_x, V_{p,x}) \quad (6)$$

$$m\ddot{y} = F_G(U_y, V_{p,y}) \quad (7)$$

$$m\ddot{z} = F_D(U_z, V_{p,z}) - W_b - P \quad (8)$$

where U_i is the component of the flow field in the i^{th} direction, $V_{p,i}$ is the component of the sphere velocity in the i^{th} direction. P is only applied when the sphere is close to the surface (within a distance ϵ). $W_b = (\rho_p - \rho_{fluid})Vg$ is the buoyant weight of the micro-sphere, with ρ_p being its density, V is its volume, ρ_{fluid} is the fluid density, and g is the gravitational acceleration. F_D is a simplified fluid drag model for a sphere in a free stream [38], which is used for z -directed forces, and is computed as:

$$F_D \approx 6\pi\mu R(U - V_p) \quad (9)$$

Since the low Reynold's number in the experiments in this work indicates Stokes flow, where inertial effects can be ignored, the inclusion of accelerations in (6)-(8) is not necessary. However, for a more generalized solution valid over a larger range of Reynold's numbers, the accelerations are included.

C. Simulation

The fluid flow caused by the Mag- μ Bot's translation is calculated by finite element modeling (FEM) using COMSOL Multiphysics (COMSOL Inc.). A Stokes-flow solution is utilized, resulting in the fluid velocity at every point in the simulation space. The Mag- μ Bot is modeled as remaining stationary at an angle of $\pi/8$ radians with respect to the surface (an approximate average angle of the Mag- μ Bot during its stick slip locomotion), and a bounding box defines the simulation space. The front and rear bounding faces are treated as a flow inlet and outlet, respectively, with a flow of 0.4 mm/s (an average Mag- μ Bot velocity from the experiments). The ground is treated as a moving wall with tangential velocity equal to the free flow velocity. All other external bounding surfaces have a symmetry condition applied, which only permits tangential flow at these boundaries. Along all faces of the Mag- μ Bot, a no-slip boundary condition was used. To reduce computational expense, half the Mag- μ Bot is simulated, taking advantage of flow symmetry. Finally, the flow velocities are reduced by 0.4 mm/s, which changes the reference frame to the case where a Mag- μ Bot is moving in a stagnant fluid.

Figure 5 shows the fluid velocity caused by the Mag- μ Bot. Fluid velocity is much higher at points closer to the micro-robot.

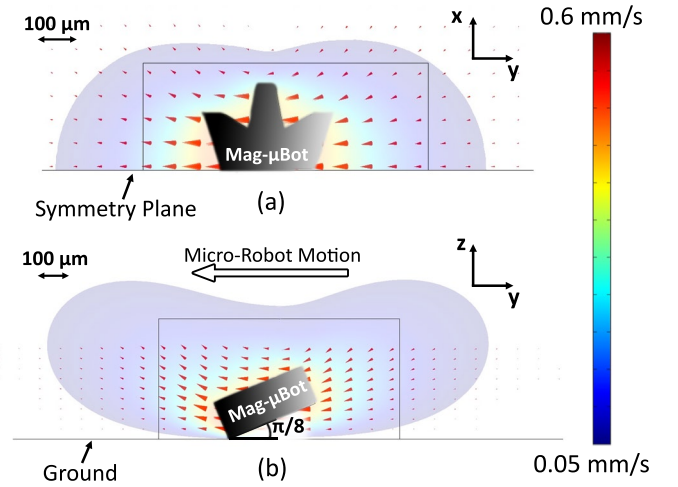


Fig. 5. (a) Top view and (b) side view slices of the finite element modeling (FEM) solution for the flow around a star-shaped Mag- μ Bot as it traverses through the environment. The Mag- μ Bot is moving towards the left in these images, and the flow velocities correspond to y -directed flow, depicted by arrows. Half the Mag- μ Bot is modeled in FEM.

The particle dynamics model from (6)-(8) is used with the flow fields computed from FEM solution to predict the displacement of a micro-sphere in 3-D. A Runge-Kutta solver (ODE23s in MATLAB, Mathworks Inc.) is used to integrate the accelerations, resulting in the displacements.

D. Simulation Results

For the case of front-pushing, we are interested in the fluid induced displacement of the micro-sphere ($D_{p,r}$) when the Mag- μ Bot leaves the sphere, after it has been positioned. This $D_{p,r}$ can be used as a controller compensation term. In the simulation, the micro-sphere is initially in contact with the front face of the Mag- μ Bot, which then moves backwards.

In the experiments, $D_{p,r} \approx 300 \pm 75 \mu\text{m}$ (over five trials). In the simulation, $D_{p,r} = 127 \mu\text{m}$, and P was not found to significantly affect results for the values determined in Sec. IV-A (subsequently, P is taken to be zero). Since the simulated $D_{p,r}$ is smaller than the experimental $D_{p,r}$, a larger friction and adhesion force would not improve the estimation, as this would further reduce $D_{p,r}$. The discrepancy between the experiment and simulation can be due to unmodeled adhesion and contact effects between the micro-robot and micro-sphere, insufficient mesh resolution close to the micro-robot (limited by computational resources), or due to only using the velocity of the fluid flow at the micro-sphere's center, which may not be representative for the entire sphere. However, the model-based predicted displacement values can be used as an initial estimate for an autonomous front-pushing controller. Additionally, because of the high variability in the experimental results for $D_{p,r}$, the method of contact-pushing may not be suitable for fine positioning of objects.

For the case of side-pushing, D_g is varied to determine its effect on D_s in both the simulations and experiments, with results shown in Fig. 6. From these results, the relation between D_g and D_s is consistent between simulation and experiment. The experiment shows slightly higher displace-

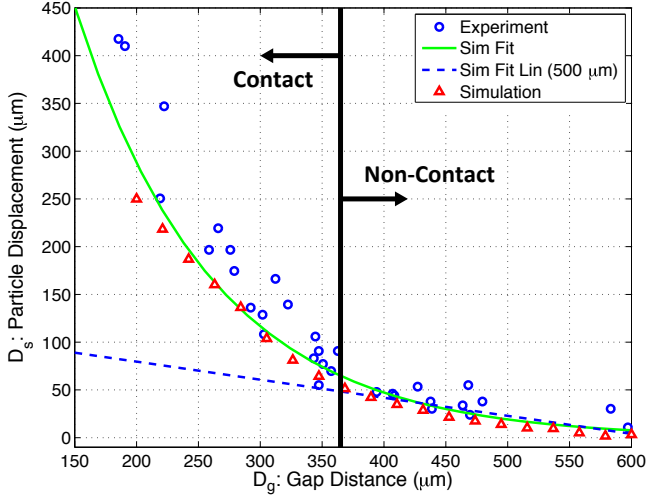


Fig. 6. Simulation and experiment of a star-shaped Mag- μ Bot manipulating a 210 μm micro-sphere from the side. Vertical division indicates whether sphere contact occurs with the micro-robot's edge, determined from the simulation. Sim Fit represents (22), and Sim Fit Lin represents (23).

ments, particularly when D_g is small and contact occurs, which can lead to additional unmodeled motion. Contact is not modeled in the simulations, but appears to only have a significant effect for $D_g < 250 \mu\text{m}$, thus minor contact may not significantly push the sphere. As the micro-robot approaches the micro-sphere from the side, fluid effects can cause the sphere to be “pulled-in” such that the gap distance shortens when the micro-robot is close to the sphere. Thus the required initial gap distance (D_g) to avoid contact will be larger than half the robots width, and the dynamic simulation is utilized to determine the actual critical gap distance. The contact threshold in Fig. 6 is at $D_g \approx 370 \mu\text{m}$, which is determined when the micro-sphere overlaps the micro-robot in the simulation.

V. MANIPULATION STRATEGIES

A. Front-Pushing Control

In front-pushing, the Mag- μ Bot attempts to position a micro-object by pushing it by direct contact to a desired position. As discussed in Sec. III and Fig. 1, the pushing process must compensate for fluid interactions to achieve accurate positioning. Figure 7 shows a schematic of the proposed pushing method in a simplified 1-D case; the micro-object (at position \mathbf{P}_s) is desired to be moved a goal position (at position \mathbf{P}_g) by the Mag- μ Bot (at position \mathbf{P}_r). The method to perform this is as follows:

- 1) The Mag- μ Bot is visually servoed to \mathbf{P}_{ri} , which is a point on the pushing line connecting \mathbf{P}_s to \mathbf{P}_g positioned behind the object.
- 2) The Mag- μ Bot moves along the line connecting \mathbf{P}_{ri} to \mathbf{P}_g , causing it to contact and push the object. The object is pushed until it reaches \mathbf{P}_o , which is determined by the relation:

$$\mathbf{P}_o(i) = \mathbf{P}_g(i) + \delta(i) \quad (10)$$

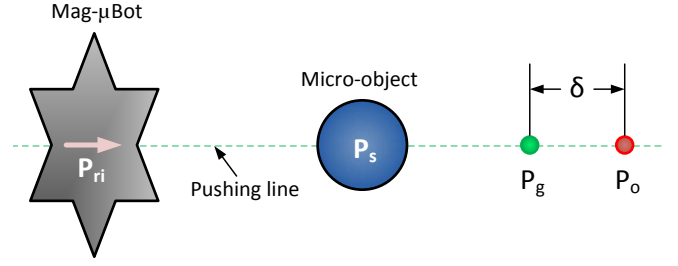


Fig. 7. Schematic of the front-pushing operation, where the Mag- μ Bot must push the micro-object to the goal position, P_g .

where i corresponds to the pushing iteration, and δ is the compensation distance. $\delta(0)$ can be initialized to the model-based predicted compensation distance, determined in Sec. IV-D, which acts as a feed-forward term.

Pushing occurs until the condition is satisfied:

$$|\mathbf{P}_s(i) - \mathbf{P}_o(i)| < \epsilon_p \quad (11)$$

where ϵ_p is a specified maximum positioning error.

- 3) The Mag- μ Bot then moves away from the object along a line that connects P_r to P_s . During this step, the object is pulled a distance $D_{p,r}$ due to fluid interactions.
- 4) At this point, if the termination condition is satisfied:

$$|\mathbf{P}_s(i) - \mathbf{P}_g(i)| < \epsilon_p \quad (12)$$

then the pushing process can terminate. Otherwise the process repeats with an integrator to update δ , giving the control law:

$$\delta(i+1) = \delta(i) + K_c [\mathbf{P}_g(i) - \mathbf{P}_s(i)] \quad (13)$$

where K_c is the gain of the controller. This controller represents an iterative learning control scheme [39].

Stability of this feedback control system can be shown by modeling it in discrete time, with every pushing iteration corresponding to a single increment in time. The resulting $D_{p,r}$ in each iteration is not time or input dependent, thus is a 0th ordered plant. Thus we can analyze the open loop system, $G_{ol}(z)$, as simply an integrator from (13):

$$G_{ol}(z) = \frac{K_c}{z-1} \quad (14)$$

which uses the Euler forward approximation for integration. The closed loop system, $G_{cl}(z)$, is given by:

$$G_{cl}(z) = \frac{G_{ol}(z)}{1 + G_{ol}(z)} = \frac{K_c}{z-1 + K_c} \quad (15)$$

Bounded-input, bounded-output (BIBO) stability is satisfied if the poles of (15) lie inside the unit circle [40], imposing the condition: $0 < K_c < 2$. Furthermore, $K_c = 1$ represents the critically damped system, suggesting the optimum gain.

B. Side-Pushing Control

To efficiently use side pushing to position an object, it is desirable to implement the model that relates D_g to D_s , determined in Sec. IV-D from physical models, in a pushing controller. Figure 8 displays a simplified schematic of the proposed pushing process, where the object is being pushed to \mathbf{P}_g . The algorithm proposed to perform this is as follows:

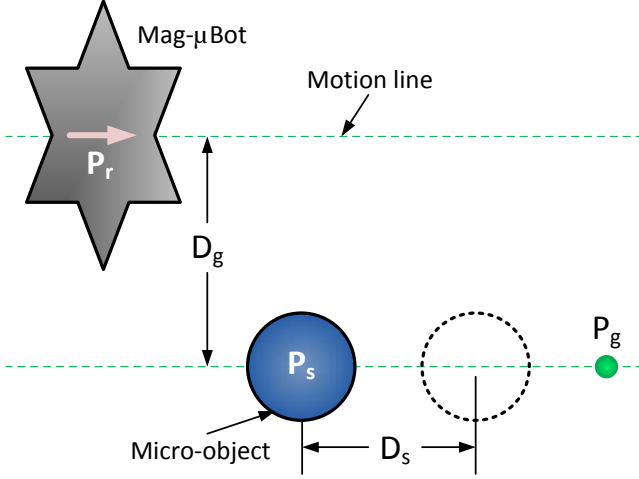


Fig. 8. Schematic of the side-pushing operation, where the Mag- μ Bot must push the micro-object to the goal position, \mathbf{P}_g .

- 1) The desired object displacement, $D_{s,des}(i)$ is determined:

$$D_{s,des}(i) = \mathbf{P}_g(i) - \mathbf{P}_s(i) \quad (16)$$

and subsequently, the corresponding gap distance between the micro-robot and object, $D_{g,est}(i)$ is computed:

$$D_{g,est}(i) = \mathcal{F}_{lin} [D_{s,des}(i) + \Delta(i)] \quad (17)$$

where \mathcal{F}_{lin} is a linearized model of \mathcal{F} , which is the function that relates D_g to D_s , and can be determined from Fig. 6. \mathcal{F} can be appropriately bounded to a minimum D_g value that avoids robot-object contact, and correspondingly, $D_{s,des}(i)$ is bounded. $\Delta(i)$ is a correction term determined from feedback; $\Delta(0) = 0$ initially.

- 2) The Mag- μ Bot proceeds to move along its motion line, which is a distance $D_{g,est}(i)$ from the line connecting $\mathbf{P}_s(i)$ to $\mathbf{P}_g(i)$, and parallel to it, as shown in Fig. 8. Afterwards, $D_{s,act}(i)$, the actual object displacement, is measured from the visual feedback information.
- 3) Next, $\Delta(i+1)$ is computed using $D_{s,act}(i)$ to improve the performance of the next pushing attempt:

$$\Delta(i+1) = \Delta(i) + K_s [D_{s,act}(i) - D_{s,des}(i)] \quad (18)$$

where K_s is the integration gain for this controller.

- 4) If the termination condition (12) is satisfied, the pushing process is complete, otherwise it is repeated.

Considering each pushing attempt is a single increment in time, stability of this system can be determined by considering

the relation between the input to this controller, $D_{s,des}$, to the output, $D_{s,act}$. This gives the open loop system $H_{ol}(z)$:

$$H_{ol}(z) = \frac{K_s}{z-1} \cdot \mathcal{F}_{lin} \cdot \mathcal{F}_{act}^{-1} \quad (19)$$

where \mathcal{F}_{act} represents the actual relation between D_g and D_s , and is not necessarily known or constant. Similar to (15), the closed loop system $H_{cl}(z)$ is:

$$H_{cl}(z) = \frac{K_s \cdot \mathcal{F}_{lin} \cdot \mathcal{F}_{act}^{-1}}{z-1 + K_s \cdot \mathcal{F}_{lin} \cdot \mathcal{F}_{act}^{-1}} \quad (20)$$

and is BIBO stable with the condition: $0 < K_s \cdot \mathcal{F}_{lin} \cdot \mathcal{F}_{act}^{-1} < 2$. The better the model estimation \mathcal{F}_{lin} matches the real system, i.e. $\mathcal{F}_{lin} \cdot \mathcal{F}_{act}^{-1} \rightarrow 1$, the more convenient it is to define a K_s that will ensure stability.

C. Autonomous Two-Particle Assembly

A proposed method to assemble two micro-objects using a Mag- μ Bot is shown in Fig. 9, which aims to avoid undesirable fluid displacements, shown in Fig. 3. The algorithm to perform the assembly is as follows:

- 1) The *Adjusted line* is defined as a line that is at an angle θ_n to the line connecting \mathbf{P}_{s1} to \mathbf{P}_{s2} .
- 2) The *Motion line* is created, which is parallel to the *Adjusted line*, a distance D_g from it.
- 3) The Mag- μ Bot is moved along the *Motion line*, which results in side-pushing of micro-object 1, and moves it towards micro-object 2.
- 4) If the two micro-objects are in contact, then assembly is completed, otherwise the process must repeat. Contact can be determined by detecting a collision between the two objects. For the simple case of a sphere:

$$|\mathbf{P}_{s2} - \mathbf{P}_{s1}| \leq R_{ms1} + R_{ms2} + \epsilon_{as} \quad (21)$$

satisfies the termination condition, where R_{ms1} and R_{ms2} are the radii of micro-object 1 and 2, respectively, and ϵ_{as} is an error tolerance of assembly.

This proposed assembly method essentially utilizes side-pushing to perform the assembly, which avoids the undesirable $D_{p,r}$ if front-pushing is utilized for assembly. However, front-pushing can be utilized to initially bring micro-object 1 near micro-object 2 (as in Fig. 3), which is generally a faster process than side-pushing.

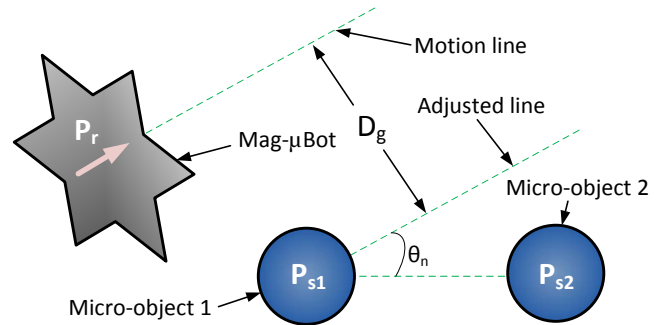


Fig. 9. Schematic of the assembly operation, where the Mag- μ Bot must assemble micro-objects 1 and 2.

VI. EXPERIMENTS AND DISCUSSION

In each of the experiments, the Mag- μ Bot is utilized to position a $210\ \mu\text{m}$ micro-sphere to a goal location. To maintain experimental conditions among different trials, the Mag- μ Bot is first manually positioned to a point $1\ \text{mm}$ away from the micro-sphere, which is far enough such that fluid motion caused by the micro-robot does not measurably affect the sphere. Once the positioning task is initiated, the goal location is specified to be $750\ \mu\text{m}$ further away from the sphere in the front-pushing case, and $300\ \mu\text{m}$ away in the side-pushing case. In side-pushing, the micro-robot will first automatically move onto the motion line to maintain a particular D_g while pushing.

In side-pushing, after the end of a pushing iteration, the Mag- μ Bot must move to a new initial position before beginning the next iteration. To do this, it moves away and around the sphere at a distance of at least $650\ \mu\text{m}$ (from Fig. 6, this distance does not significantly disturb the micro-sphere) to a position on the motion line (from Fig. 8) that is $1\ \text{mm}$ further ‘behind’ the micro-sphere, with respect to the goal.

A. Front-Pushing

To analyze the effectiveness of the proposed front-pushing strategy discussed in Sec. V-A, experiments are performed where the Mag- μ Bot pushes a $210\ \mu\text{m}$ micro-sphere to a goal location using the proposed controller with varying K_c and $\delta(0)$; these results are presented in Fig. 10, which displays the number of successfully converged trials as a function of pushing attempts. Ten experimental trials are attempted for each controller, with up to ten pushing attempts. Within each trial, the pushing algorithm is repeated until the sphere is within $\epsilon_p = 75\ \mu\text{m}$ of the goal position, after which the operation is stopped. The number of repetitions is shown in Fig. 11, which displays a representative experiment for each controller.

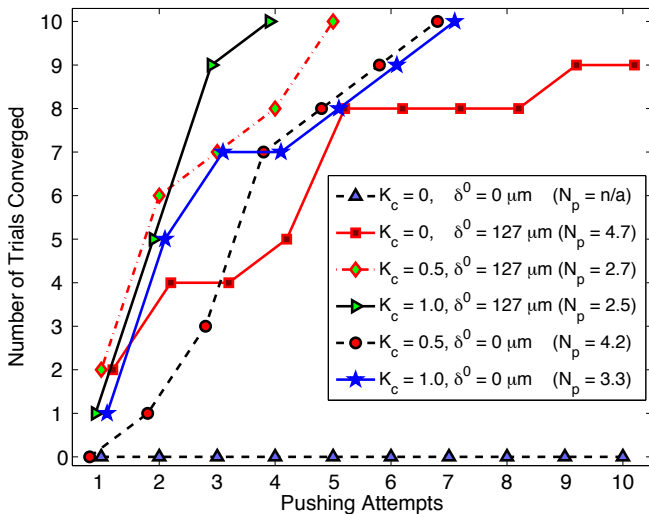


Fig. 10. Experimental front-pushing convergence as a function of pushing attempts for the different controllers; up to 10 pushing attempts are shown. For each controller, 10 pushing trials are performed. N_p is the overall average number of pushing attempts to push the object to its goal location, within the allowed error tolerance of $\epsilon_p = 75\ \mu\text{m}$.

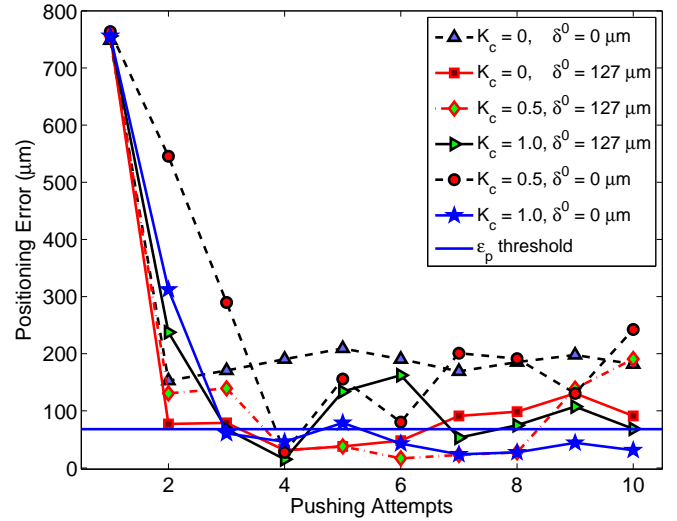


Fig. 11. Experimental positioning error during front-pushing as a function of pushing attempts different controller parameters. A single, typical experiment is represented by each controller, up to 10 pushing attempts. The ϵ_p termination threshold is shown, which is used for the experiments in Fig. 10; $\epsilon_p = 0$ is used in these experiments to demonstrate the limitations of front-pushing for fine positioning.

From these results, it is apparent that positioning within the specified ϵ_p is not possible when $K_c = 0$ and $\delta(0) = 0$, which is the naïve case where the model-based estimate and iterative controller are not used. A steady state error of about $200\ \mu\text{m}$ is achieved, although one would expect the error to be about $300\ \mu\text{m}$, which corresponds to the $D_{p,r}$ that actually occurs. However, the micro-robot overshoots the goal position by about $100\ \mu\text{m}$ due to the visual servoing controller being slightly under-damped, which is due to a constant micro-robot translational velocity being used, as well as a time lag caused by image processing.

If a model-based $\delta(0)$ is used without the iterative controller ($K_c = 0$), convergence is possible, but may take many pushing attempts to occur. This would imply that due to variability, $D_{p,r} \approx \delta$ in many cases in actual experiments. This can occur because the micro-sphere is not always in complete contact with the front face of the Mag- μ Bot when it moves away, which leads to a smaller $D_{p,r}$, and can be combined with the overshoot the micro-robot applies to the sphere from its motion control scheme.

For the results that use the iterative controller ($K_c > 0$), convergence occurs quicker for $K_c = 1$, which is the critically damped case, as opposed to $K_c = 0.5$, an overdamped case. Combining the controller with the model-based $\delta(0)$ further improves convergence by about 1 iteration, supporting its viability in the pushing control scheme. The average error over pushing attempts using the best controller is shown in Fig. 14.

Additional errors in pushing can arise from non-idealities in the environment, such as any dirt or contamination on certain areas of the workspace affecting the micro-robot or micro-objects. Also, the actual pushing task takes place in a 2-D environment, while the pushing control scheme assumes only 1-D motion; deviation from the pushing line induces additional errors, which may delay convergence.

B. Side-Pushing

To analyze the effectiveness of the proposed side-pushing strategy discussed in Sec. V-B, experiments are performed where the Mag- μ Bot pushes a 210 μm micro-sphere (without contact) to a goal location using the iterative controller with varying parameters. K_s is varied with a linearized model of \mathcal{F} , and is compared to non-learning models ($K_s = 0$), as well as to naïve controllers where D_g is kept constant. These results are presented in Fig. 12, which displays the number of successfully converged trials as a function of pushing attempts. Ten experimental trials are attempted for each controller, with up to 30 pushing attempts. Additionally, Fig. 13 displays the positioning error as a function of pushing attempts for a representative experiment for each controller. In the experiments, the Mag- μ Bot is maintained a distance of at least 650 μm from the micro-sphere when it is not performing the pushing process, for example, when resetting to a new initial pushing position. The micro-sphere is pushed to a tolerance of $\epsilon_p = 7.5 \mu\text{m}$ (corresponding to 1 pixel on the image).

In the experiments, \mathcal{F} is taken from the Simulation data in Fig. 6, which is most representative of the experimental results. An exponential curve fit is performed and inverted, giving the empirical relation:

$$\mathcal{F}(D_s) = -\frac{1}{0.009042} \ln\left(\frac{D_s}{1755}\right) \quad [\mu\text{m}] \quad (22)$$

which fits the data with $R^2 = 0.9971$. \mathcal{F} is linearized about $D_s = 500 \mu\text{m}$ (a typical non-contact pushing distance), giving the relation:

$$\mathcal{F}_{lin}(D_s) = -5.29D_s + 621 \quad [\mu\text{m}] \quad (23)$$

Equations (22) and (23) are also displayed in Fig. 6.

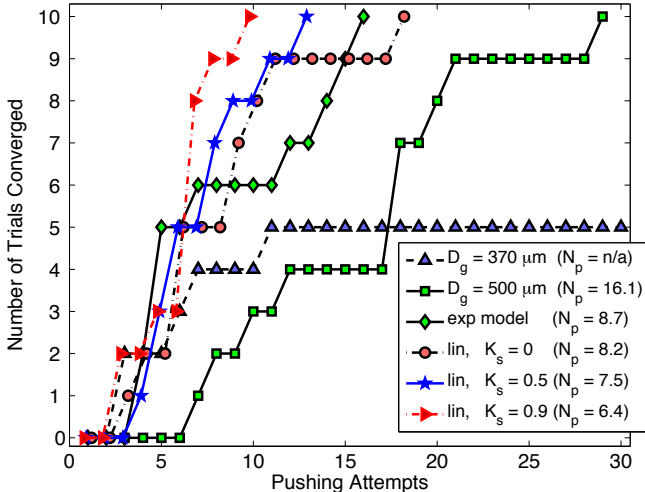


Fig. 12. Experimental side-pushing convergence as a function of pushing attempts different controller parameters. For each controller, 10 pushing trials are performed. N_p is the overall average number of pushing attempts to push the object to its goal location, within the allowed error tolerance of $\epsilon_p = 7.5 \mu\text{m}$. ‘exp’ corresponds to the model from (22), and ‘lin’ corresponds to the model from (23).

From the results in Fig. 12, it is apparent that using a model-based solution with the iterative controller provides the

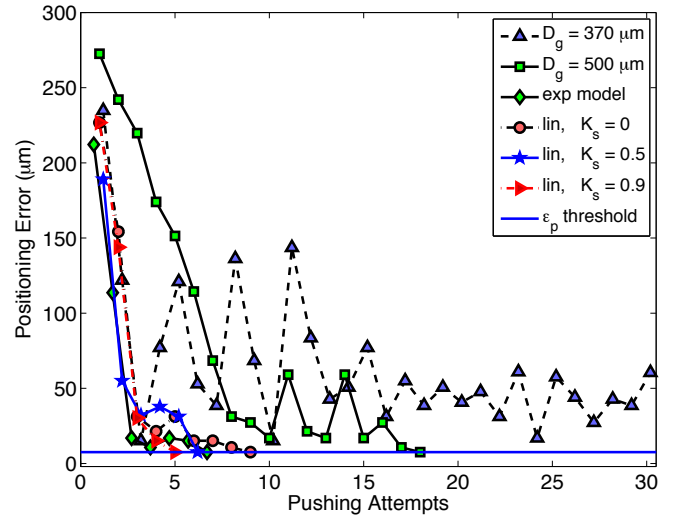


Fig. 13. Positioning error during side-pushing as a function of pushing attempts different controller parameters. A single, typical experiment is represented by each controller.

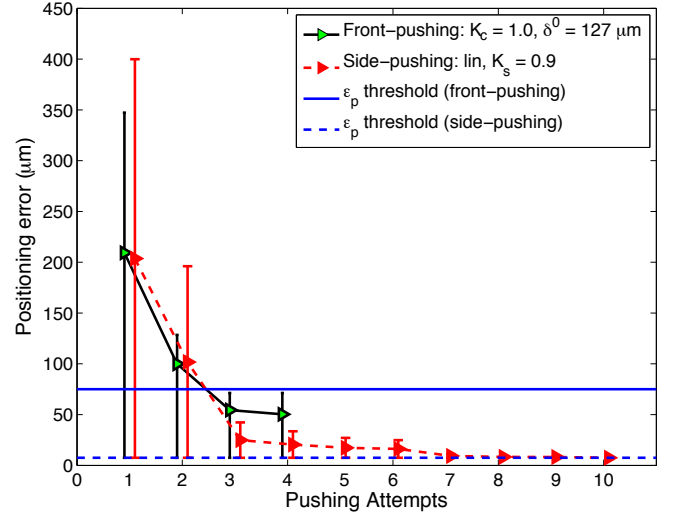


Fig. 14. Average positioning error as a function of pushing attempts for the best front-pushing and side-pushing controllers. All experiments are within the specified ϵ_p after 4 attempts for front-pushing, and 10 attempts for side-pushing.

fastest convergence. For the naïve case where $D_g = 370 \mu\text{m}$, convergence can occur early by chance, but will fail to converge after 30 attempts in many cases. This is highlighted by oscillatory behavior in positioning error, as seen in Fig. 13, which is due to the micro-robot over-pushing the sphere due to an insufficiently large D_g . For $D_g = 500 \mu\text{m}$, the sphere can be positioned within 30 attempts in all cases, however is inefficient because small displacements are realized in every iteration, but may still be too large when the sphere is very close to its target position.

Using the model-based relation between D_g and D_s improves the convergence rate of the sphere to its target position, with minor differences between the exponential function (22), and the linearized function (23). The linear model is slightly better in this regard, as the exponential function can slightly

over-push the sphere when it is close to its target, being slightly under-damped. The linear model represents a slightly over-damped controller, and more conservatively pushes the sphere to its target for small displacements.

Adding the iterative learning controller further improves positioning convergence. The $K_s = 0.5$ experiment represents an over-damped controller, while the $K_s = 0.9$ is closer to being critically damped, and thus converges slightly faster. The average error over pushing attempts using the best controller is shown in Fig. 14.

The actual value K_s for critical damping depends on the accuracy of \mathcal{F}_{lin} to the actual system; if the accuracy is perfect, then $K_s = 1.0$ for critical damping. From Fig. 6, it is apparent that the model and experiment match closely, and $K_s = 0.9$ was used to attempt to achieve the critically damped condition: $K_s \mathcal{F}_{lin} \cdot \mathcal{F}_{act}^{-1} = 1$. Additionally, the learning controller can be improving performance as it can correct for any non-ideal changes in the environment. For example, if the micro-sphere gets stuck on a piece of dirt during manipulation, its response to the micro-robot's motion can change significantly, which the controller can compensate for. Another case that can make non-corrective models non-convergent is if the Mag- μ Bot's motion becomes impeded such that it cannot accurately follow its motion paths (and thus not satisfy the requested D_g); this can occur due to environmental non-idealities such as contamination, or the micro-robot itself may have non-ideal properties that causes it to deviate from paths in certain conditions.

C. Autonomous Two-Particle Assembly

To demonstrate the proposed micro-object assembly strategy from Sec. V-C, a star-shaped Mag- μ Bot is tasked with assembling two $\approx 210 \mu\text{m}$ micro-spheres together. This experiment is shown in Fig. 15, where the Mag- μ Bot first attempts to front-push MS1 to assemble with MS2, which subsequently disassembles as the Mag- μ Bot retracts. Side-pushing is then employed to complete the assembly, which is found to be a successful strategy towards achieving micro-object assembly. $\theta_n = 30^\circ$ is used and arbitrarily chosen; optimizing the assembly process will be done in future work.

For the assembly of more than two objects, further task planning will be required to successfully position and assemble objects into more intricate configurations. The effect of fluid disturbance will need to be accounted; for example, the pushing of a third micro-sphere into the assembly in Fig. 15(f) could cause the initial two-particle assembly to be broken apart due to fluid perturbations by the moving micro-robot. An approach that incorporates the physical pushing models discussed in this work could lead to predictions on how all micro-objects in the workspace will be affected by the moving micro-robot, and could be compensated for towards creating target multi-object assemblies. However, using this potential approach, the computation and complexity of the necessary micro-robot motion paths could scale poorly as the number of micro-objects increases.

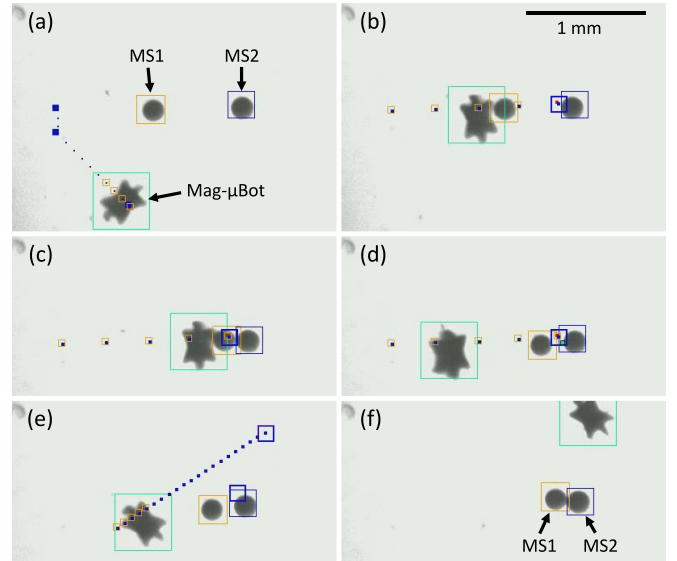


Fig. 15. A Mag- μ Bot assembling two micro-spheres, MS1 and MS2, together. (a) The Mag- μ Bot prepares to move into a position to push MS1, and (b) front-pushes it towards MS2. (c) MS1 and MS2 are assembled until the Mag- μ Bot leaves in (d), where MS1 and MS2 separate due to fluid effects. (e) The Mag- μ Bot prepares to side-push MS1; (f) after two side-pushing iterations, MS1 and MS2 are assembled. Images are enhanced for viewing.

VII. CONCLUSION AND FUTURE WORK

In this study, we addressed the challenge of manipulating micro-objects in a fluidic environment using an untethered magnetic micro-robot. Specifically, three tasks were considered: (1) front-pushing a micro-sphere using the micro-robot by direct contact, (2) side-pushing a micro-sphere using the micro-robot without contact, and (3) pushing two micro-spheres together using the micro-robot. In all three tasks, the effects of fluid flow caused by the translating micro-robot must be accounted for to successfully accomplish the tasks. We found that the performance of both front and side-pushing tasks can be improved by incorporating results from a physical simulation, as well utilizing an iterative learning scheme into the pushing controllers. For assembly, we find that using a front-pushing strategy does not successfully assemble micro-spheres, however using side-pushing, the micro-spheres can be assembled using the micro-robot.

Future works will include using the micro-robot to autonomously manipulate micro-objects of arbitrary shapes, which will require control of the micro-object's orientation. The creation of larger scale micro-object assemblies will also be investigated by an autonomous micro-robot, as well as the manipulation of the assemblies themselves.

ACKNOWLEDGMENT

The authors would like to thank William Messner for suggestions, Magnequench Inc. for supplying magnetic materials, and the NanoRobotics Laboratory members for their support. This work is supported by the National Science Foundation CAREER award program (NSF IIS-0448042).

REFERENCES

- [1] M. Sitti, "Voyage of the microrobots," *Nature*, vol. 458, no. 30, pp. 1121–1122, 2009.
- [2] M. Sitti, "Microscale and nanoscale robotics systems - characteristics, state of the art, and grand challenges," *IEEE Robotics and Automation Magazine*, vol. 14, pp. 53–60, 2007.
- [3] B. Donald, C. Levey, and I. Paprotny, "Planar microassembly by parallel actuation of mems microrobots," *Journal of Microelectromechanical Systems*, vol. 17, pp. 789–808, 2008.
- [4] M. Sakar, E. B. Steager, A. A. Juliusz, M. Kim, V. Kumar, and G. J. Pappas, "Biosensing and actuation for microrobots," in *IEEE International Conference on Robotics and Automation*, (Anchorage, AK), pp. 3141–3146, 2010.
- [5] D. R. Frutiger, K. Vollmers, B. E. Kratochvil, and B. J. Nelson, "Small, fast, and under control: Wireless resonant magnetic micro-agents," *International Journal of Robotics Research*, vol. 29, pp. 613–636, 2009.
- [6] L. Zhang, J. J. Abbott, L. Dong, B. E. Kratochvil, D. Bel, and B. J. Nelson, "Artificial bacterial flagella: Fabrication and magnetic control," *Applied Physics Letters*, vol. 94, pp. 064107–064109, 2009.
- [7] A. Yamazaki, M. Sendoh, K. Ishiyama, K. I. Arai, R. Kato, M. Nakano, and H. Fukunaga, "Wireless micro swimming machine with magnetic thin film," *Journal of Magnetism and Magnetic Materials*, vol. 272–276, pp. 1741–1742, 2004.
- [8] C. Pawashe, S. Floyd, and M. Sitti, "Modeling and experimental characterization of an untethered magnetic micro-robot," *International Journal of Robotics Research*, vol. 28, pp. 1077–1094, 2009.
- [9] A. Ghosh and P. Fischer, "Controlled propulsion of artificial magnetic nanostructured propellers," *Nano Letters*, vol. 9, pp. 2243–2245, 2009.
- [10] H. Maruyama, T. Fukuda, and F. Arai, "Laser manipulation and optical adhesion control of a functional gel-microtool for on-chip cell manipulation," in *IEEE International Conference on Intelligent Robots and Systems*, (St. Louis, MO), pp. 1413–1418, 2009.
- [11] O. Sul, M. Falvo, R. Taylor, S. Washburn, and R. Superfine, "Thermally actuated untethered impact-driven locomotive microdevices," *Applied Physics Letters*, vol. 89, pp. 203512–203514, 2006.
- [12] A. Solovev, Y. Mei, E. Urena, G. Huang, and O. Schmidt, "Catalytic microtubular jet engines self-propelled by accumulated gas bubbles," *Small*, vol. 5, pp. 1688–1692, 2009.
- [13] S. Martel, M. Mohammadi, O. Felfoul, Z. Lu, and P. Poupponeau, "Flagellated magnetotactic bacteria as controlled mri-trackable propulsion and steering systems for medical nanorobots operating in the human microvasculature," *International Journal of Robotics Research*, vol. 28, pp. 571–582, 2009.
- [14] B. Behkam and M. Sitti, "Bacterial flagella-based propulsion and on/off motion control of microscale objects," *Applied Physics Letters*, vol. 90, pp. 023902–023904, 2007.
- [15] V. Arabagi, B. Behkam, E. Cheung, and M. Sitti, "Modeling of stochastic motion of bacteria propelled spherical microbeads," *Journal of Applied Physics*, vol. 109, pp. 114702–114712, 2011.
- [16] C. Liu, C. Chiang, C. Chang, and C. Liu, "A lobster-sniffing inspired actuator for manipulation of micro-objects via controlling local fluid," *Sensors and Actuators A*, vol. 130–131, pp. 545–552, 2006.
- [17] C. Pawashe, S. Floyd, and M. Sitti, "Multiple magnetic control using electrostatic anchoring," *Applied Physics Letters*, vol. 94, pp. 164108–164110, 2009.
- [18] S. Floyd, E. Diller, C. Pawashe, and M. Sitti, "Control methodologies for a heterogeneous group of untethered magnetic micro-robots," *International Journal of Robotics Research*, DOI: 10.1177/0278364911399525, 11 March 2011.
- [19] S. Floyd, C. Pawashe, and M. Sitti, "Two-dimensional contact and non-contact micro-manipulation in liquid using an untethered mobile magnetic micro-robot," *IEEE Transactions on Robotics*, vol. 25, pp. 1332–1342, 2009.
- [20] C. Pawashe, S. Floyd, and M. Sitti, "Assembly and disassembly of magnetic mobile micro-robots towards 2-D reconfigurable micro-systems," in *Int. Symp. Robotics Research*, (Lucerne, Switzerland), 2009.
- [21] M. Arulampalam, S. Maskell, N. Gordon, and T. Clapp, "A tutorial on particle filters for online nonlinear/non-gaussian bayesian tracking," *IEEE Transactions on Signal Processing*, vol. 50, no. 2, pp. 174–188, 2002.
- [22] J.-C. Latombe, *Robot motion planning*. Kluwer Academic Publishers, 1991.
- [23] R. Fearing, "Survey of sticking effects for micro parts handling," in *IEEE/RSJ International Conference on Intelligent Robots and Systems*, (Pittsburgh, PA), pp. 212–217, 1995.
- [24] F. Arai, D. Ando, T. Fukuda, Y. Nonoda, and T. Oota, "Micro manipulation based on micro physics - strategy based on attractive force reduction and stress measurement," in *IEEE/RSJ International Conference on Intelligent Robots and Systems*, vol. 2, (Pittsburgh, PA), pp. 236–241, 1995.
- [25] J. Israelachvili, *Intermolecular and Surface Forces*. Academic Press, 1992.
- [26] M. Gauthier, S. Regnier, P. Rougeot, and N. Chaillet, "Forces analysis for micromanipulations in dry and liquid media," *Journal of Micromechanics*, vol. 3, pp. 389–413, 2006.
- [27] M. Sitti and H. Hashimoto, "Teleoperated touch feedback from the surfaces at the nanoscale: Modeling and experiments," *IEEE/ASME Transactions on Mechatronics*, vol. 8, pp. 287–298, 2003.
- [28] D. Olsen and J. Oosteraas, "The critical surface tension of glass," *Journal of Physical Chemistry*, vol. 68, p. 27302732, 1964.
- [29] S. Rhee, "Surface energies of silicate glasses calculated from their wettability data," *Journal of Materials Science*, vol. 12, pp. 823–824, 1977.
- [30] M. Samuelsson and D. Kirchman, "Degradation of adsorbed protein by attached bacteria in relationship to surface hydrophobicity," *American Society for Microbiology*, vol. 56, pp. 3643–3648, 1990.
- [31] T. Czerwicz, N. Renevier, and H. Michel, "Low-temperature plasma-assisted nitriding," *Surface and Coatings Technology*, vol. 131, pp. 267–277, 2000.
- [32] M. Yuce and A. Demirel, "The effect of nanoparticles on the surface hydrophobicity of polystyrene," *European Physics Journal*, vol. 64, pp. 493–497, 2008.
- [33] "Solid surface energy data (sfe) for common polymers." <http://www.surface-tension.de/solid-surface-energy.html>.
- [34] F. Heslot, A. Cazabat, P. Levinson, and N. Fraysse, "Experiments on wetting on the scale of nanometers: Influence of the surface energy," *Physical Review Letters*, vol. 65, pp. 599–602, 1990.
- [35] B. Persson, *Sliding Friction: Physical Principles and Applications*. Springer, 2000.
- [36] A. Goldman, R. Cox, and H. Brenner, "Slow viscous motion of a sphere parallel to a plane wall-ii couette flow," *Chemical Engineering Science*, vol. 22, pp. 653–660, 1967.
- [37] M. King and D. Leighton Jr., "Measurement of the inertial lift on a moving sphere in contact with a plane wall in a shear flow," *Physical Fluids*, vol. 9, pp. 1248–1255, 1997.
- [38] B. Munson, D. Young, and T. Okiishi, *Fundamentals of Fluid Mechanics, 4th Edition*. John Wiley and Sons, Inc., 2002.
- [39] D. A. Bristow, M. Tharayil, and A. G. Alleyne, "A survey of iterative learning control," *IEEE Control Systems Magazine*, vol. 26, no. 3, pp. 96–114, 2006.
- [40] N. S. Nise, *Controls Systems Engineering*. John Wiley and Sons, 2004.



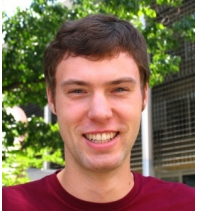
Chytra Pawashe (S'09) received the B.S., M.S., and Ph.D. degrees in mechanical engineering from Carnegie Mellon University, Pittsburgh, PA, USA, in 2006, 2008, and 2010 respectively. He is at Intel Corporation since 2011. His interests include micro/nanoscale manipulation and assembly, controls and automation, and MEMS/NEMS.

Dr. Pawashe received the second prize in the World RoboCup Nanogram Demonstration (2007), and the best paper award at IEEE IROS (2009).



Steven Floyd (S'04) received the B.S. degree in mechanical engineering (*summa cum laude*) from Washington University in St. Louis, St. Louis, MO, in 2005 and the M.S. and Ph.D. degrees in mechanical engineering from Carnegie Mellon University, Pittsburgh, PA, in 2008 and 2010, respectively. He is at Areté Associates since 2010. His interests include robotic design, MEMS, analog electronics design, and magnetic power transfer and actuation.

Dr. Floyd received the National Science Foundation Graduate Research Fellowship (2005), the second prize in the World RoboCup Nanogram Demonstration (2007), and the best paper award at IEEE IROS (2009).



Eric Diller (S'10) received the B.S. and M.S. degrees in mechanical engineering from Case Western Reserve University in Cleveland, OH, in 2009. He is currently a PhD candidate in mechanical engineering at Carnegie Mellon University. His interests include magnetic actuation, microscale manipulation, and biologically-inspired systems.



Metin Sitti (S'94-M'00-SM'08) received the B.Sc. and M.Sc. degrees in electrical and electronics engineering from Bogazici University, Istanbul, Turkey, in 1992 and 1994, respectively, and the Ph.D. degree in electrical engineering from the University of Tokyo, Tokyo, Japan, in 1999. He was a research scientist in the Department of Electrical Engineering and Computer Sciences, University of California at Berkeley during 1999-2002. He is currently an associate professor in the Department of Mechanical Engineering and Robotics Institute at Carnegie Mel-

lon University. He is the director of the NanoRobotics Laboratory, where his research interests include miniature mobile robots down to the micron-scale, biologically inspired micro/nanosystems, and micro/nano-scale manipulation and manufacturing systems.

He has been appointed as the Adamson Career Faculty Fellow in 2007, and is nominated for the World Technology Award in 2009. He received the National Science Foundation CAREER award and the Carnegie Mellon Struminger award in 2005. He was elected as the Distinguished Lecturer of the IEEE RAS from 2006-2008. He received the second prize in the World RoboCup Nanogram Demonstration (2007), the best biomimetics paper award in the IEEE ROBIO (2004), the best paper award at IEEE IROS (1998, 2009), and the best video award in the IEEE Robotics and Automation Conference (2002). He is the Vice President of Technical Activities in the IEEE Nanotechnology Council for 2008-2010, the co-editor-in-chief of the Journal of Micro/Nano-Mechatronics, and an associate editor for IEEE T-RO.